

Properties of asymmetric magnetic reconnection

J. Birn,^{1,a)} J. E. Borovsky,¹ and M. Hesse²

¹Los Alamos National Laboratory, Los Alamos, New Mexico 87545, USA

²NASA/Goddard Space Flight Center, Greenbelt, Maryland 20771, USA

(Received 10 December 2007; accepted 5 February 2008; published online 12 March 2008)

Properties of magnetic reconnection are investigated in two-dimensional, resistive magnetohydrodynamic (MHD) simulations of current sheets separating plasmas with different magnetic field strengths and densities. Specific emphasis is on the influence of the external parameters on the reconnection rate. The effect of the dissipation in the resistive MHD model is separated from this influence by evaluating resistivity dependence together with the dependence on the background parameters. Two scenarios are considered, which may be distinguished as driven and nondriven reconnection. In either scenario, the maximum reconnection rate (electric field) is found to depend on appropriate hybrid expressions based on a magnetic field strength and an Alfvén speed derived from the characteristic values in the two inflow regions. The scaling compares favorably with an analytic formula derived recently by Cassak and Shay [Phys. Plasmas **14**, 102114 (2007)] applied to the regime of fast reconnection. An investigation of the energy flow and conversion in the vicinity of the reconnection site revealed a significant role of enthalpy flux generation, in addition to the expected conversion of Poynting flux to kinetic energy flux. This enthalpy flux generation results from Ohmic heating as well as adiabatic, that is, compressional heating. The latter is found more important when the magnetic field strengths in the two inflow regions are comparable in magnitude. © 2008 American Institute of Physics.

[DOI: 10.1063/1.2888491]

I. INTRODUCTION

Magnetic reconnection is the key process in the transfer of magnetic flux, particles, and energy across magnetic boundaries, such as the magnetopause enveloping the Earth's magnetosphere, and is generally considered the main mechanism for the fast release of energy in solar flares and magnetospheric substorms (see, e.g., Ref. 1). One of the key problems in understanding the effects of magnetic reconnection is the question what determines the magnitude of the reconnection rate, that is, the magnitude of the electric field at the reconnection site or, equivalently, the rate of transfer of magnetic flux, which governs the fast energy release and regulates the energy and flux transfer through the magnetic boundary. In simple two-dimensional models, where the plasma properties in the two inflow regions are identical and differ only by opposite magnetic field orientations, the reconnection rate can be written as

$$E_r = f v_A B_0, \quad (1)$$

where B_0 is the magnetic field strength in either inflow region, $v_A = B_0 / \sqrt{\mu_0 \rho_0}$ is the Alfvén speed in the inflow region, and f is a numerical factor much smaller than unity. In the simplest incompressible models, the density ρ_0 in the inflow region is the same as at the reconnection site and in the outflow region, so that a distinction between these densities is not necessary. In compressible models, these densities may differ, and it is not *a priori* clear on which density the Alfvén speed should be based.

In these simple configurations the dependence of the reconnection rate E_r on B_0 and ρ_0 from the scaling is trivial, and the nontrivial investigation concerns the magnitude of the factor f . In classical resistive magnetohydrodynamic (MHD) models of reconnection the magnitude of f is controlled by the magnitude of the resistivity η . For instance, in the steady-state Sweet–Parker model,^{2,3} f is proportional to $\eta^{1/2}$. This power law results from the underlying assumption that the accelerated plasma, ejected from the reconnection site at the Alfvén speed, crosses through a thin extended diffusion region, in which the dissipation takes place. In contrast, in Petschek's model of fast reconnection,⁴ most of the acceleration takes place at slow shocks extending from the reconnection site, while the actual diffusion region is considerably smaller. The Petschek model permits a much higher reconnection rate, which depends only weakly (logarithmically) on the resistivity and may reach $f \approx 0.1$. Note that in general, the factor f may also depend on the scaling parameters as well as on other factors, such as system size.

Resistive MHD simulations (e.g., Ref. 5) tend to favor the Sweet–Parker regime, unless the resistivity is large and strongly localized.⁶ In contrast to typical resistive models, numerical simulations of collisionless reconnection have demonstrated that magnetic reconnection in sufficiently thin current sheets, in which Hall effects and ion particle dynamics become important, may occur at a fast rate with $f \approx 0.1$, which apparently does not depend on the dissipation mechanism (e.g., Ref. 7). Similar rates can be obtained also from resistive MHD models when the resistivity is localized, either imposed directly⁸ or implicitly from a current density

^{a)}Electronic mail: jbirn@lanl.gov.

dependence,⁹ and assumes large values, corresponding to a small Lundquist number,

$$S = \mu_0 L_0 v_A / \eta, \quad (2)$$

of order unity. Here L_0 is a characteristic length scale, for instance, the initial (half) thickness of the current sheet undergoing reconnection.

While the scaling of the reconnection rate E_r with B_0 and ρ_0 may be considered trivial in a standard current sheet model with antiparallel fields of the same magnitude and symmetric densities, it is no longer trivial when these quantities differ on the two sides of the current sheet. Reconnection in such asymmetric configurations has been investigated recently by Refs. 10–12, all using resistive MHD.

Cassak and Shay¹⁰ used a Sweet–Parker-type analysis to derive scaling laws for the reconnection rate (and other parameters) for antiparallel reconnection between plasmas of different magnetic field strength and density. Their result is given by Eq. (1) with a hybrid magnetic field strength and Alfvén speed defined by (using MKS units)

$$B_0 = \sqrt{B_1 B_2}, \quad (3)$$

$$v_A = \sqrt{\frac{B_1 B_2}{\mu_0 \rho_0}}, \quad (4)$$

where

$$\rho_0 = \frac{B_1 \rho_2 + B_2 \rho_1}{B_1 + B_2} \quad (5)$$

represents an estimate for the density in the outflow region. A factor

$$f \propto S^{-1/2} \quad (6)$$

was obtained consistent with Sweet–Parker scaling for small resistivity (large S). This leads to a reconnection rate given by

$$E_r \sim \sqrt{\frac{\eta v_A}{\mu_0 L} B_1 B_2}. \quad (7)$$

Their result was verified in resistive MHD simulations of reconnection for the special case of initially uniform density.¹⁰

Borovsky and Hesse¹¹ studied nondriven antiparallel reconnection initiated by a resistive “spot” in the center of a large box, using identical magnetic field strengths on both sides of the current sheet but different densities with a ratio varying between 1 and 320. Their imposed localized resistivity corresponds to a relatively small Lundquist number of order unity. In this regime the Sweet–Parker scaling for small resistivity, Eq. (6) is no longer appropriate. A more adequate scaling can be obtained from Eq. (18) of Ref. 10 (here modified for MKS units)

$$E_r \sim \frac{2\delta}{L} v_A \frac{B_1 B_2}{B_1 + B_2} \quad (8)$$

by setting $\delta/L = f \approx 0.1$, consistent with Petschek scaling. (Here δ and L are the half-width and the half-length of the dissipation region, respectively.) In that case, Eq. (1) applies

with v_A given by Eq. (4) and a hybrid magnetic field strength given by

$$B_0 = \frac{2B_1 B_2}{B_1 + B_2} \quad (9)$$

instead of Eq. (3), and a constant factor f . (The two expressions for B_0 become identical, however, for $B_1 = B_2$, as considered by Ref. 11.) Using a more precise factor $f = 0.07$, Borovsky and Hesse¹¹ found a reasonable agreement of the reconnection rates in their simulations with those predicted by the Cassak–Shay formula (8) with v_A given by Eq. (4), which, for $B_1 = B_2 = B_0$, is reduced to

$$v_A = \frac{B_0}{\sqrt{\mu_0(\rho_1 + \rho_2)/2}}. \quad (10)$$

A slightly better agreement with the simulations was found when the average density in Eq. (10) was replaced by

$$\rho_{av} = \frac{5}{8}\rho_1 + \frac{3}{8}\rho_2, \quad (11)$$

weighing the lower density more heavily. Note, however, that there was no theoretical justification of Eq. (11) and that the symmetry of the formulas between regions 1 and 2 is lost in that case.

The simulations in Ref. 11 were motivated by studying the effects of high-density plasmaspheric plasma on reconnection at the nose of the magnetosphere. A more direct investigation of magnetopause reconnection by Borovsky *et al.*¹² used the facilities at the Community Coordinated Modeling Center (CCMC) at NASA/Goddard Space Flight Center to study reconnection rates in a global solar wind-magnetosphere system. This study used high-resolution 3D MHD simulations based on the BATS-RUS code. A resistive spot was added at the frontside magnetopause to ensure fast controlled reconnection. In this scenario, reconnection may be considered as “driven” by the impact of the solar wind. A parameter range of reconnection rates was explored by varying the solar wind speed gradually for two sets of solar wind fields and density, representing high and low Mach numbers, respectively. In these simulations, both density and magnetic field strength varied between inside and outside the magnetopause. In all cases, good agreement with the Cassak–Shay formula (8) was found, applied to the fast reconnection regime of large resistivity with S of order unity.

In the present paper we will further investigate the dependence of the reconnection rate on the external parameters B_0 and v_A in configurations that are not symmetric, such that both B and ρ values differ in the two inflow regions. Furthermore, the external parameters may also influence the factor f in Eq. (1), specifically in resistive MHD through the Lundquist number (2). Therefore, we will consider the dependence of the reconnection rate on the external parameters together with the resistivity dependence.

We will consider two scenarios which may be distinguished as “driven” and “nondriven.” The first scenario is based on the “Newton challenge” problem,¹³ which consists of magnetic reconnection in a plane current sheet, forced by temporally limited inflow into the system. This results in a compression equivalent to the consequence of a finite defor-

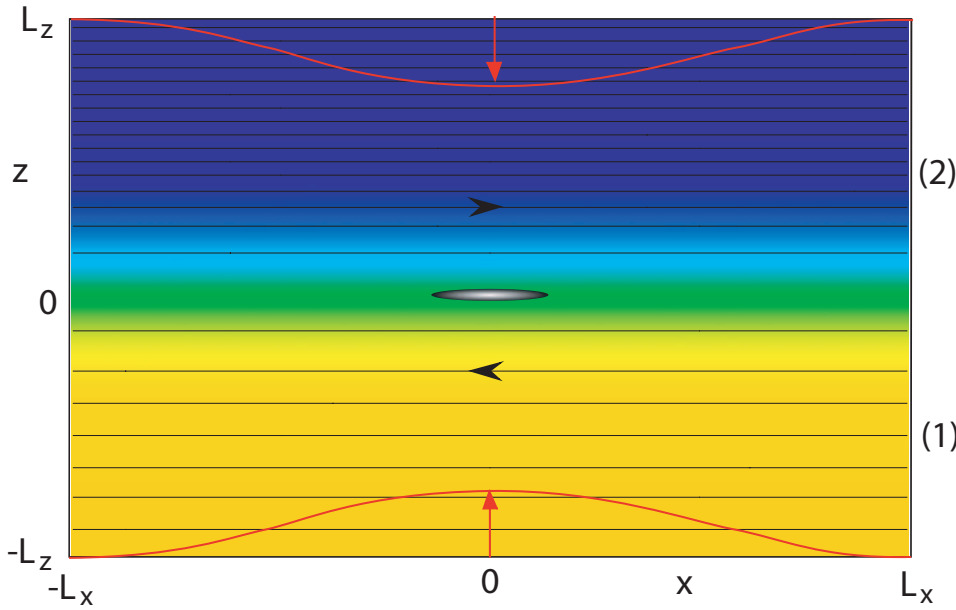


FIG. 1. (Color) Initial configuration, consisting of a plane current sheet with different magnetic field strengths and densities on the two sides. Solid black lines are magnetic field lines with the higher field strength on side 2. Color indicates plasma density. The shaded oval in the center indicates a resistive “spot,” located at $x=0$ and $B_x=0$, which may move in time. For one set of simulations a finite inflow was employed at $z = \pm L_z$, leading to a deformation of the external fields indicated by the red lines; for details, see text.

mation of the boundary. The second scenario is the unforced growth of a tearing instability initiated by imposing a localized spot of high resistivity, similar to the approach of Ref. 11. To reduce the stabilizing effects of a finite system, we will consider a box much larger than in the first scenario. We note that we use the term “driven” for the first scenario somewhat loosely to indicate a potentially strong influence but not necessarily one that results in a quasisteady state.

We will again address the reconnection problem from the one-fluid MHD approach. Although for many space scenarios a kinetic approach seems more appropriate, the fluid limit seems sufficient to explore the dependence of the reconnection rate on the external parameters. In Sec. II we present the initial states and the numerical approach. Before dealing with the proper scaling of the reconnection rate in Sec. V we will first present characteristics of the temporal evolution in Sec. III and of the flow associated with different asymmetric configurations in Sec. IV. This is followed by details of the energy budget in Sec. VII and a summary and discussion in Sec. VIII.

II. INITIAL STATES AND NUMERICAL APPROACH

In the following we will use dimensionless quantities, based on the magnetic field strength on side 2, B_2 , the density on side 1, ρ_1 , and the half-thickness of the current sheet, L_c , with other units given by appropriate combinations of these, for instance, velocity $v_c = B_2 / \sqrt{\mu_0 \rho_1}$, time $t_c = L_c / v_c$, pressure $p_c = B_2^2 / \mu_0$, and electric field $E_c = v_c B_2$.

The initial current sheet configuration consists of a shifted Harris-type magnetic field profile, illustrated by Fig. 1. The initial magnetic field is given by

$$B_x = [\tanh(z - b) + b] / (1 + b), \quad (12)$$

$$B_y = B_z = 0, \quad (13)$$

where b is a parameter smaller than unity, regulating the difference between the field strengths on the two sides, such that the external field approaches $B_x = -(1 - b) / (1 + b)$ on side

1 and $B_x = 1$ on side 2. This parameter was also chosen as an offset in the hyperbolic tangent function in Eq. (12), so that the initial location of $B_x = 0$ was near $z = 0$. For magnetopause applications one might identify the, higher-magnetic-field, side 2 with the magnetosphere and side 1 with the magnetosheath near the nose of the magnetosphere. Note that our coordinates are not the magnetospheric ones appropriate for this region. Here we use coordinates with x along the field that reverses sign across the current sheet, z perpendicular to the current sheet and y in the invariant direction.

The corresponding plasma pressure follows from pressure balance; it is given by

$$p = \frac{1}{2}(1 - B_x^2) + p_b, \quad (14)$$

where an arbitrary background pressure p_b is included. The plasma density was chosen as

$$\rho = 1 + (\rho_2 - 1)(1 - \lambda^2), \quad \lambda = \frac{1}{2}[1 + \tanh(z - b)], \quad (15)$$

varying smoothly between $\rho_1 = 1$ and ρ_2 , which may be smaller or larger than ρ_1 .

The reconnection problem outlined above was studied by a MHD code,¹⁴ using nonuniform grids with up to 400² grid cells and a localized resistivity model given by

$$\eta = \eta_1 / \cosh^2 r, \quad r = \sqrt{(x/d_x)^2 + [(z - z_x)/d_z]^2}, \quad (16)$$

centered at the (varying) location of the magnetic null (x -point) $x = 0$, $z = z_x$, where $B_x = 0$ and $B_z = 0$. The grid size and the number of grid points were varied to ensure that they did not affect the results.

Two scenarios were considered, which may be distinguished as “driven” and “non-driven.” The first scenario is based on the “Newton challenge” problem,¹³ which consists of magnetic reconnection forced by temporally and spatially localized inflow into the exterior regions at $z = \pm L_z$ given by

$$v_z = \mp \hat{v}(t) \cos^2(\pi x / 2L_d) \quad \text{for } z = \pm L_z, \quad (17)$$

$$\hat{v}(t) = d\zeta/dt = 2a\omega \tanh(\omega t) / \cosh^2(\omega t), \quad (18)$$

TABLE I. Initial parameters for four characteristic cases.

Case	b	B_1/B_2	ρ_2/ρ_1	v_{A1}	v_{A2}	p_1	p_2	β_1	β_2	s_1	s_2
A	0.8	0.111	0.4	0.111	1.581	0.594	0.1	96	0.2	0.732	0.628
B	0.8	0.111	10	0.111	0.316	0.594	0.1	96	0.2	0.732	0.025
C	0.2	0.667	0.4	0.667	1.581	0.373	0.1	1.68	0.2	0.553	0.628
D	0.2	0.667	10	0.667	0.316	0.373	0.1	1.68	0.2	0.553	0.025

$$\zeta(t) = a \tanh^2(\omega t). \quad (19)$$

The inflow speed and hence the boundary electric field reach a maximum at $\omega t \approx 0.65$ and subside after $\omega t \approx 2.5$.

Symmetry boundary conditions were employed at $x=L_x$ and at $x=0$. The parameters $a=1$ and $\omega=0.1$ and the background pressure $p_b=0.1$ were chosen to be the same as in the Newton challenge problem. The box size in this case was also the same as in the Newton challenge problem, given by

$$L_x = 8, \quad L_z = 4. \quad (20)$$

The scales for the localized resistivity were chosen as

$$d_x = 2, \quad d_z = 1. \quad (21)$$

For the nondriven problem, without inflow, we chose a much larger box size to reduce the effects of boundary stabilization

$$L_x = 100, \quad L_z = 40 \quad (22)$$

and

$$d_x = 5, \quad d_z = 1 \quad (23)$$

for the localized resistivity, choosing the same parameters as Ref. 11, except for the box size in x , which is 1/2 of their box length. We also did runs with an extended box size in x but found no difference in the maximum reconnection rates.

The relatively large size of the resistive spot relative to the box size in the driven case was chosen to be consistent with the choices for the Newton challenge simulations,¹³ as well as to give a similar size relative to the current sheet width as the nondriven problem. However, we also performed driven simulations with a smaller resistive spot. They led to similar results with the same scaling results as discussed in Sec. V and are therefore not presented here.

To contrast various parameter regimes and to identify the proper scaling of the reconnection rate, we chose four parameter sets, given in Table I, for both driven and nondriven simulations. Here $v_{Ai} = B_i / \sqrt{\rho_i}$ ($i=1, 2$) is the Alfvén speed in either inflow region, p_i is the pressure, $\beta_i = 2p_i / B_i^2$, and $s_i = p_i^{1/\gamma} / \rho_i$ are a measure of entropy density, where $\gamma=5/3$ is the adiabatic index (ratio of specific heats). We note that the values given in Table I are the asymptotic values for large $|z|$. The actual values at the boundaries of the small box are slightly lower.

III. CHARACTERISTIC EVOLUTION AND VALIDITY TESTS

Figure 2 illustrates the evolution of a nondriven run (case C), showing magnetic field lines (solid black lines) and the velocity component v_x (color scale) for a simulation with a localized resistivity given by Eq. (16) with $\eta_1=0.5$, $d_x=5$, $d_z=1$. After initiation of reconnection by imposing the finite resistivity, the region of fast flow propagates outward from the reconnection site, whereas the vicinity of the reconnection site appears to remain relatively steady. The fast outflow is highly asymmetric, flowing predominantly into the region of high magnetic field strength, lower pressure, or (more significantly, as we will see later) higher Alfvén speed.

The evolution of the reconnected flux (given by the increase of magnetic flux in the outflow, or reduction of magnetic flux in the inflow, regions) and the reconnection rate for this case is shown in Fig. 3. The reconnection rate (bottom panel) is evaluated in two ways, by the value of ηj_y at the x -line (solid line) and by the temporal change of the reconnected flux (dashed line). Both show excellent agreement. This test is used in our simulations to ensure consistence of the calculated reconnection rates. If the simulations are not sufficiently resolved, numerical diffusion might ensue and the two values are found to differ.

We further studied the influence of the box size in x on the reconnection rates. Figure 4 shows the evolution of reconnected flux and reconnection rate, now for driven runs with initial parameters $B_1/B_2=0.5$, $\rho_2/\rho_1=1$, using a resistivity with $\eta_1=0.01$, $d_x=2$, $d_z=1$. The driving inflow was the same for all runs, given by Eq. (17) with $L_d=8$; however, the system size in x was varied between $L_x=8$ and $L_x=32$. While the late results differ somewhat, the behavior around the maximum reconnection rate is very similar, aside from a slight reduction of the peak for $L_x=8$. This demonstrates that our peak reconnection rates, to be considered in Sec. V, are not affected by the finite size of the outflow region. We did not investigate the effects of varying the inflow here, because an earlier investigation of the symmetric Newton challenge problem¹³ found that these effects could be accounted for by the proper scaling with the field parameters in the inflow region.

IV. FLOW CHARACTERISTICS

Figures 5 and 6 provide a comparison of the flow characteristics for 4 nondriven cases A–D, as defined by Table I, choosing $\eta_1=0.5$. Only a central part of the simulation box is shown in each case, near the time of maximum reconnection

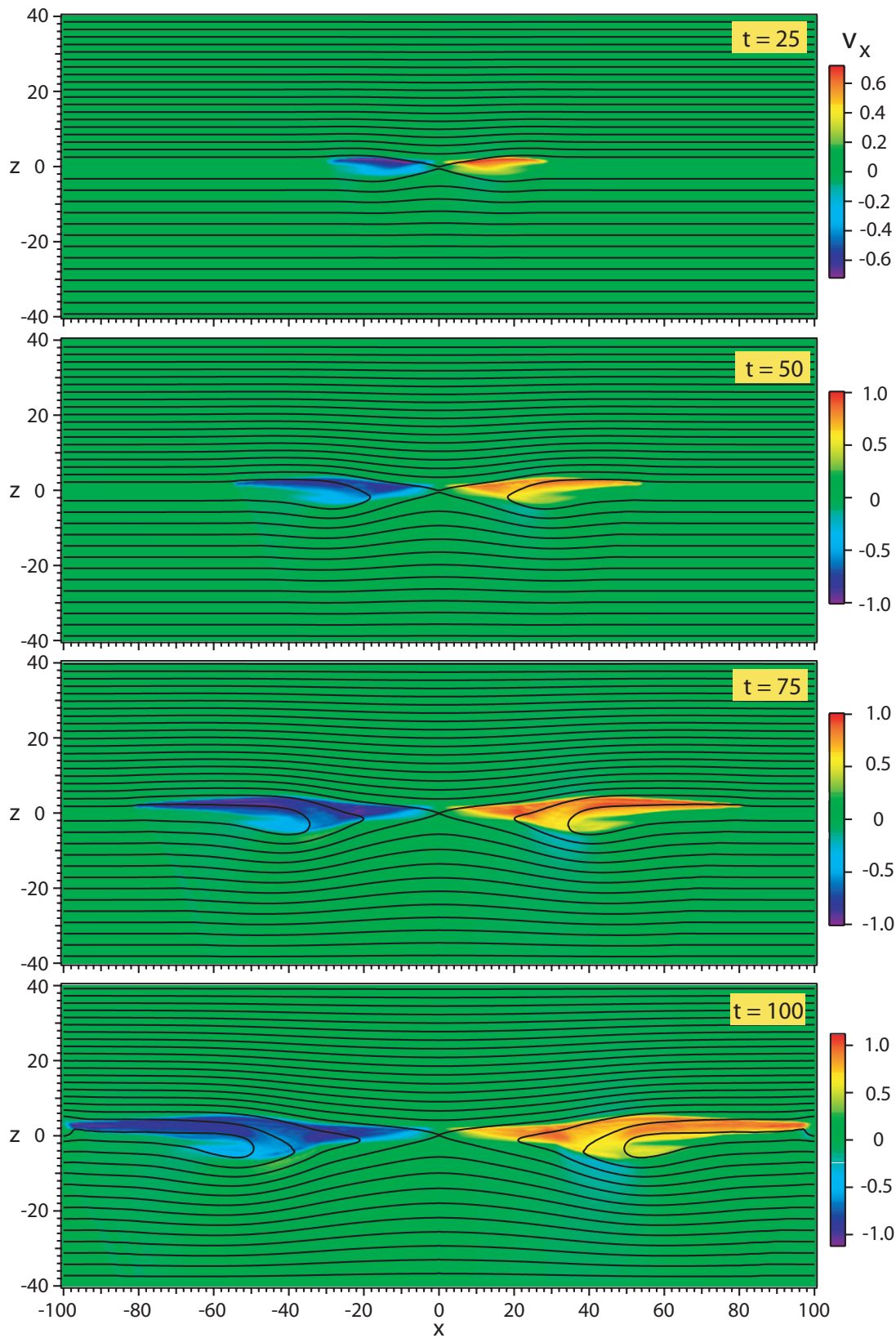


FIG. 2. (Color) Evolution of a nondriven run (case C), showing magnetic field lines (solid black lines) and the velocity component v_x (color scale) for a resistive MHD simulation with a localized resistivity given by Eq. (16) with $\eta_l=0.5$, $d_x=5$, $d_z=1$.

rate ($t=120, 150, 40, 60$ for cases A, B, C, D, respectively). Figure 5 shows the velocity component v_x (color) together with magnetic field lines (solid black lines). Thin white contours show contours of η_j , indicating the diffusion region.

In relation to the x-line, the diffusion region is shifted towards region 2 with the larger magnetic field, because the gradient of B_x and hence the current density are shifted in this direction (whereas the resistivity is centered on $B_x=0$).

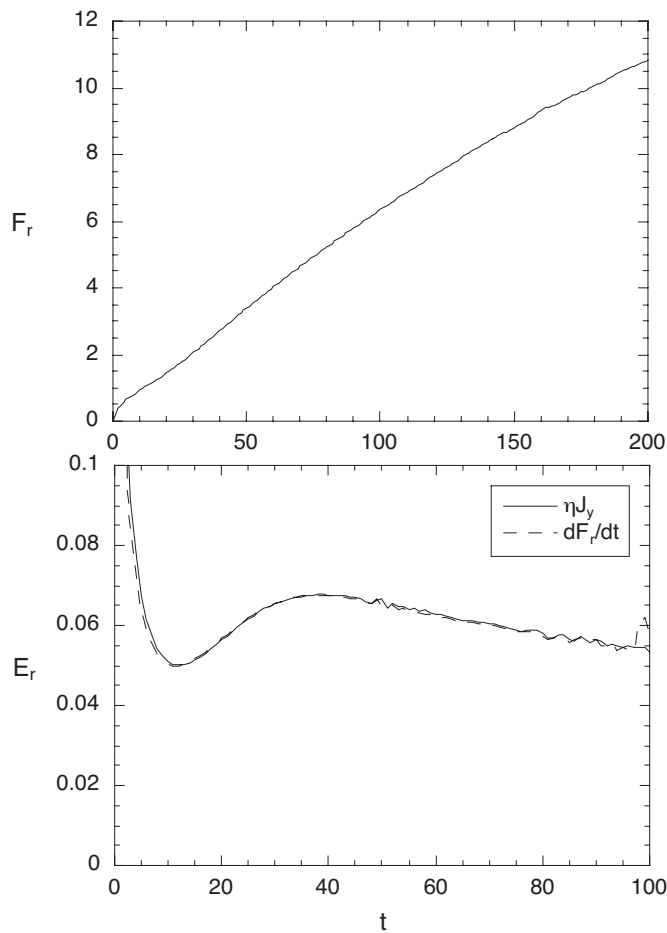


FIG. 3. Evolution of the reconnected flux (top) and the reconnection rate (bottom) for a nondriven run (case C) with a localized resistivity given by Eq. (16) with $\eta_1=0.5$, $d_x=5$, $d_z=1$. The reconnection rate in the bottom panel is evaluated in two ways, by the value of ηj_y at the reconnection site (solid line) and by the temporal change of the reconnected flux (dashed line).

Heavy colored lines indicate plasma paths that lead from $t=0$ (small circles) into the region of fast outflow. Figure 6 shows the corresponding densities (color), again together with the plasma trajectories.

Clearly the fast outflow is asymmetric in each case, going into region 2 in cases A–C, but into region 1 in case D. As shown by Table I, the common property of the outflow region for the fast flows is the higher magnitude of the Alfvén speed, rather than the magnetic field strength or lower density.

The heavy traces in Figs. 5 and 6, together with the density in Fig. 6, indicate the origin of the plasma contributing to the fast outflow. In cases A, B, and D we find that the origin is region 1. Case C is more complicated. The trajectories farther to the right [white in Fig. 5(c), red in Fig. 6(c)], which contribute to the front of the fast beam, originate from region 2, but rather than entering the outflow region by moving towards negative z , the plasma elements enter through expansion of the outflow region. The trajectories farther to the left [blue in Figs. 5(c) and 6(c)] mainly originate from region 1. The common property of the origins appears to be higher entropy density or, for the later contributions to the

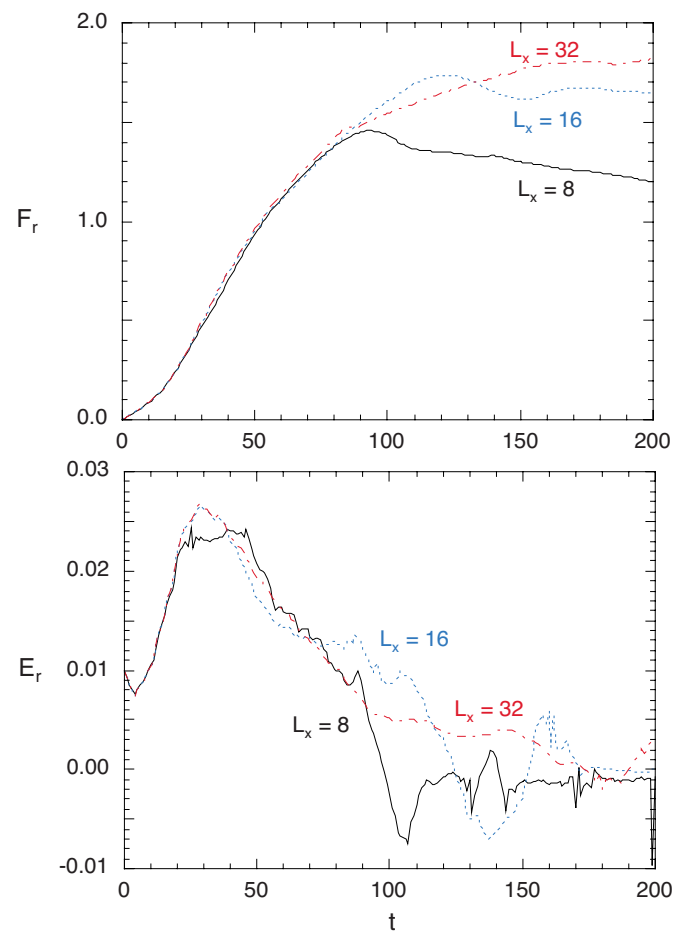


FIG. 4. (Color online) Evolution of the reconnected flux (top) and the reconnection rate (bottom) for a driven run with a localized resistivity given by Eq. (16) with $\eta_1=0.01$, $d_x=2$, $d_z=1$, for three different box lengths L_x . The inflow was the same in all cases, confined to $|x| < 8$.

fast flows, higher pressure and lower magnetic field strength.

The flow evolution of the driven cases is not shown here. At early times we find a behavior consistent with that of the nondriven cases, fast outflow into the region of higher Alfvén speed, originating primarily from the regions of higher entropy density or higher pressure. At later times the flow pattern becomes more complicated, due to the smaller size of the simulation box, which leads to reflections and oscillations.

V. SCALING OF RECONNECTION RATES

As discussed in Sec. I, the reconnection rate in the resistive regime depends not only on the external parameters in the inflow regions but also on the magnitude of resistivity. This dependence is demonstrated in Fig. 7(a), which shows the maximum reconnection rates E_R as a function of the resistivity amplitude η_1 , defined in Eq. (16), for both driven and nondriven simulations A–D, defined in Table I and Eqs. (20)–(23). As shown by the right panel of Fig. 7(a), for large values of η_1 of the order of unity, the reconnection rates saturate and become largely independent of resistivity. For smaller resistivity we find a dependence varying between

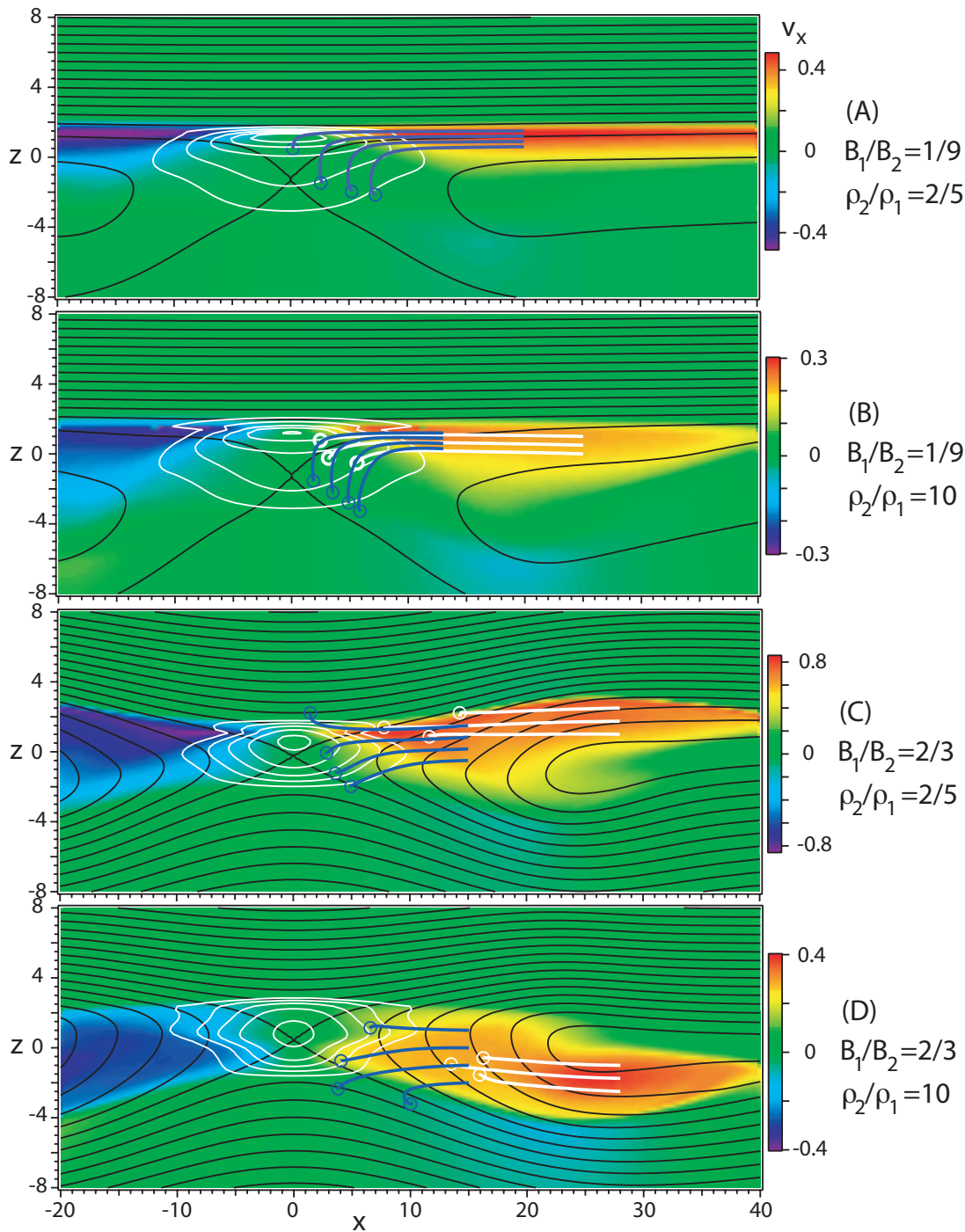


FIG. 5. (Color) Comparison of the flow characteristics for nondriven runs A–D at the times of maximum reconnection rate, using localized resistivity given by Eq. (16) with $\eta_1=0.5$. Only a central part of the simulation box is shown, with magnetic field lines (solid black lines) and the velocity component v_x (color scale). Thin white contours show contours of η_j , indicating the diffusion region. Heavy blue and white lines indicate plasma paths that lead from a location at $t=0$ (small circles) into the region of fast outflow.

approximately $\eta^{1/3}$ and $\eta^{1/2}$ for the driven cases (left panel), the latter consistent with Sweet–Parker scaling. For the nondriven cases this regime was not explored.

The deviation of the curves in Fig. 7(a) from each other demonstrates that our chosen initial normalization, based on B_2 and ρ_1 does not provide the appropriate scaling of the reconnection rates, otherwise the curves should match. We therefore renormalized both reconnection rates and resistivity in different ways, shown in Figs. 7(b) and 7(c) for driven

and nondriven runs A–D, using the instantaneous values of B and ρ in the inflow regions at the times of the maximum reconnection rate. For the small box in the driven cases these values were taken at the boundaries, while for the larger box in the nondriven cases they were taken just outside the diffusion region, where both B_x and ρ assumed flat plateaus as a function of z . (Replacing these with the values at the boundaries did not lead to significant changes in the results.)

The curves in Fig. 7(b) are based on the normalization

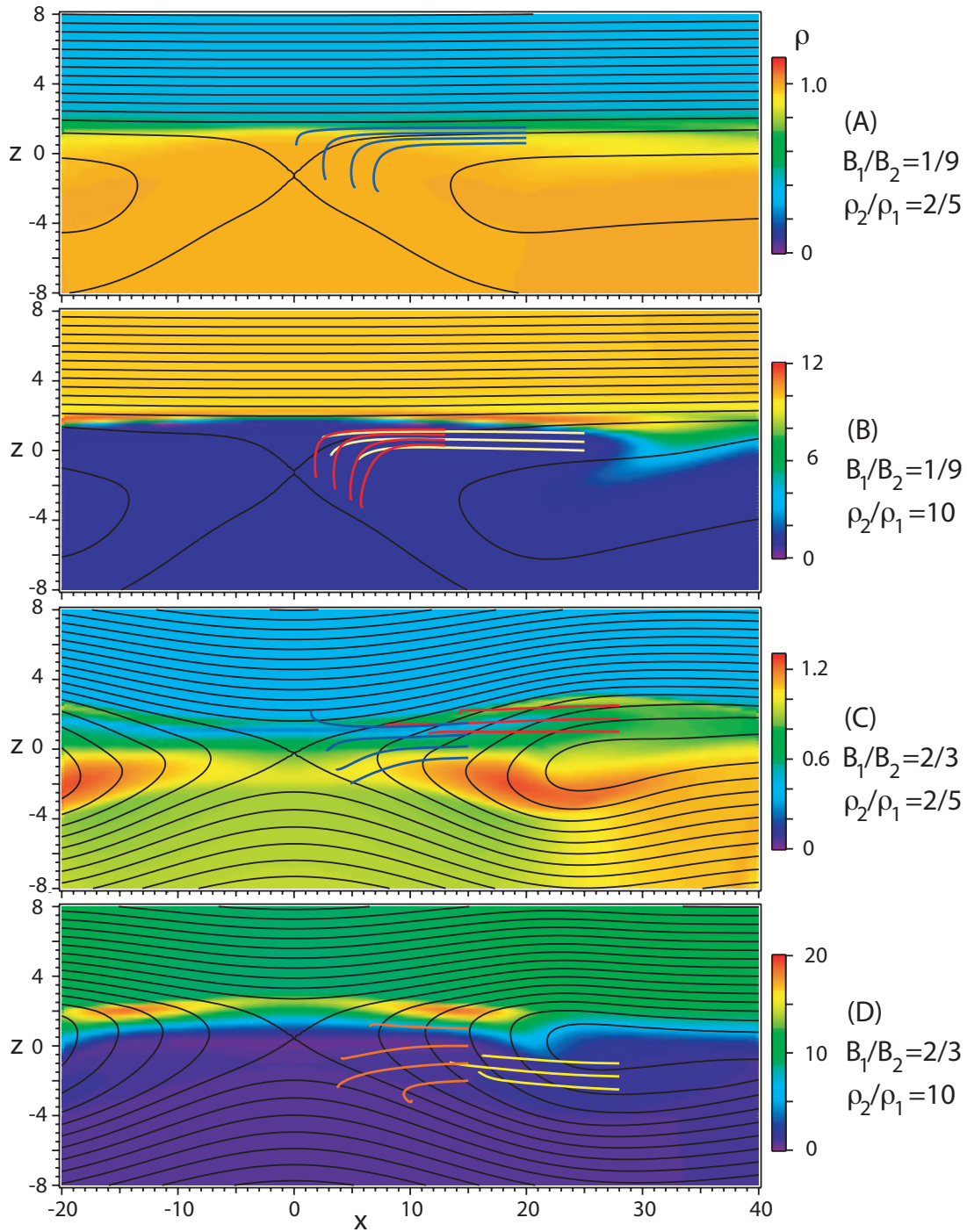


FIG. 6. (Color) Same as in Fig. 5 but showing the density (color). Plasma trajectories into the region of fast outflow are again shown as heavy colored lines.

derived by Ref. 10, using an Alfvén speed defined by Eqs. (4) and (5) and a magnetic field strength defined by Eq. (9), appropriate for large resistivity. This leads to a scaling electric field (in dimensionless units)

$$E_{N2} = \frac{2(B_1 B_2)^{3/2}}{\sqrt{(B_1 + B_2)(B_1 \rho_2 + B_2 \rho_1)}}. \quad (24)$$

The results using this scaling are clearly improved. However, Fig. 7(c) demonstrates that a further improvement can be made when the Alfvén speed for the normalization is based on the actual density ρ_x at the reconnection site, rather than

the estimated outflow density given in Eq. (5), which leads to the following scaling electric field:

$$E_{N3} = \frac{2(B_1 B_2)^{3/2}}{(B_1 + B_2)\sqrt{\rho_x}}. \quad (25)$$

This further improvement may be taken as an indication that the density at the x-line is a better estimate of the outflow density than Eq. (5). One might expect that additional improvement could be made if this density were replaced by the actual outflow density. However, it is difficult to obtain a

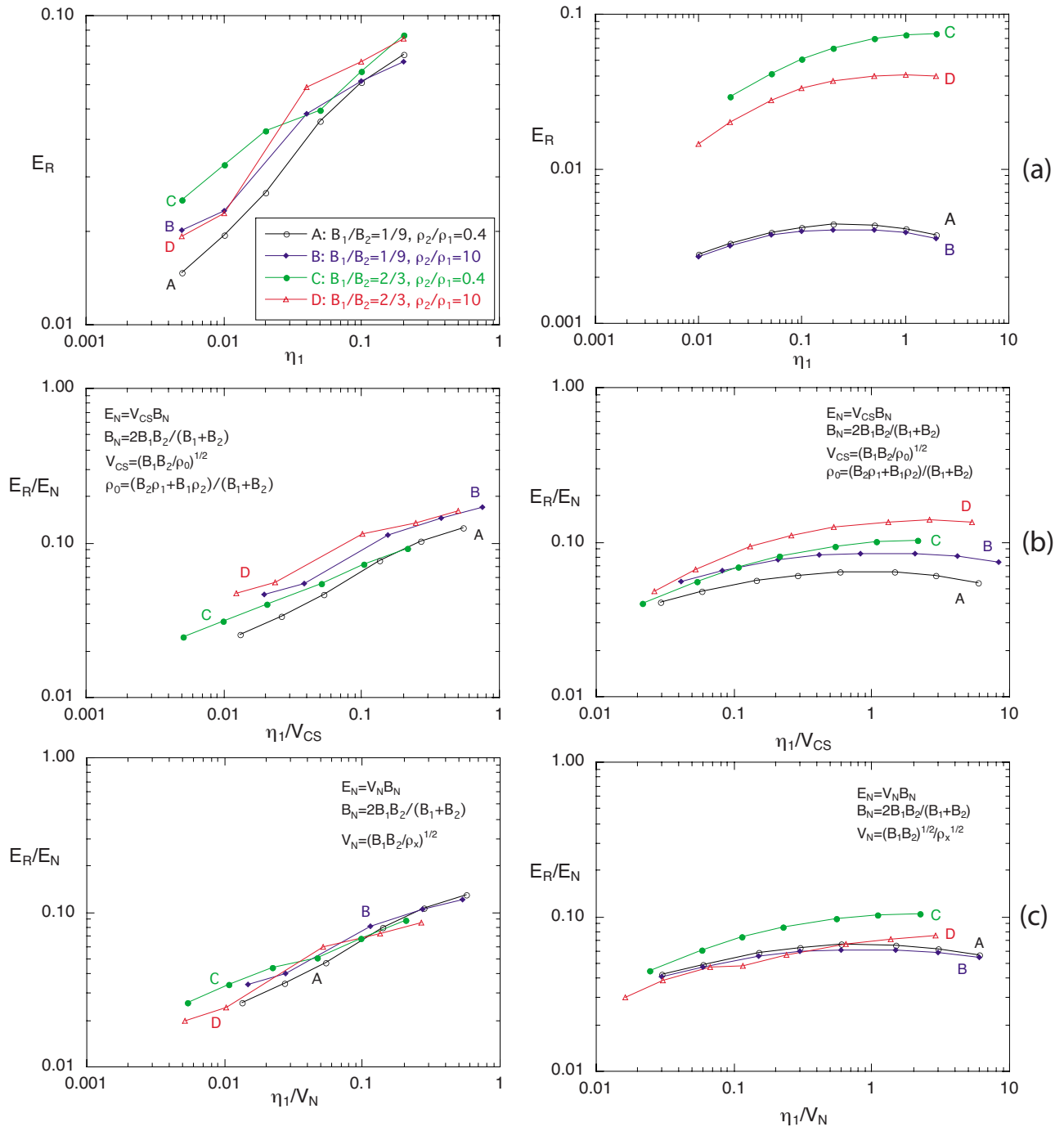


FIG. 7. (Color online) Maximum reconnection rates as a function of resistivity for (left) driven and (right) nondriven cases A–D and different normalizations indicated in the figure. The top panels correspond to our initial scaling. The center panels are based on Eq. (24), representing the Cassak–Shay formula (8) applied to the high-resistivity regime, and the reconnection rates in the bottom panels are scaled with Eq. (25), using the same formula but with an Alfvén speed based on the actual density ρ_x at the reconnection site.

well-defined outflow density because of the inhomogeneity of the outflow shown in Fig. 6.

VI. ELECTRIC FIELD IN THE DIFFUSION REGION

In a similar fashion as in Ref. 10 we investigate the contributions to the electric field E_y in the vicinity of the reconnection site and the diffusion region at the times of maximum reconnection rate. Figure 8 shows, for the non-

driven cases A–D and a resistivity $\eta_1=0.5$, the total electric field $E_y(z)$ at $x=0$ (solid red lines) and the contributions from $-\mathbf{v} \times \mathbf{B}$ (dotted green lines) and ηj_y (dashed blue lines). Crosses indicate the locations of the x-point ($B_x=0$) and the flow stagnation point ($v'_z=v_z-v_{0z}=0$).

Since the x-line is not static but varies its location along the z axis, the electric field ought to be evaluated in the frame of the moving x-line. We have done this in two ways: (a) By using the instantaneous phase speed of the moving x-line,

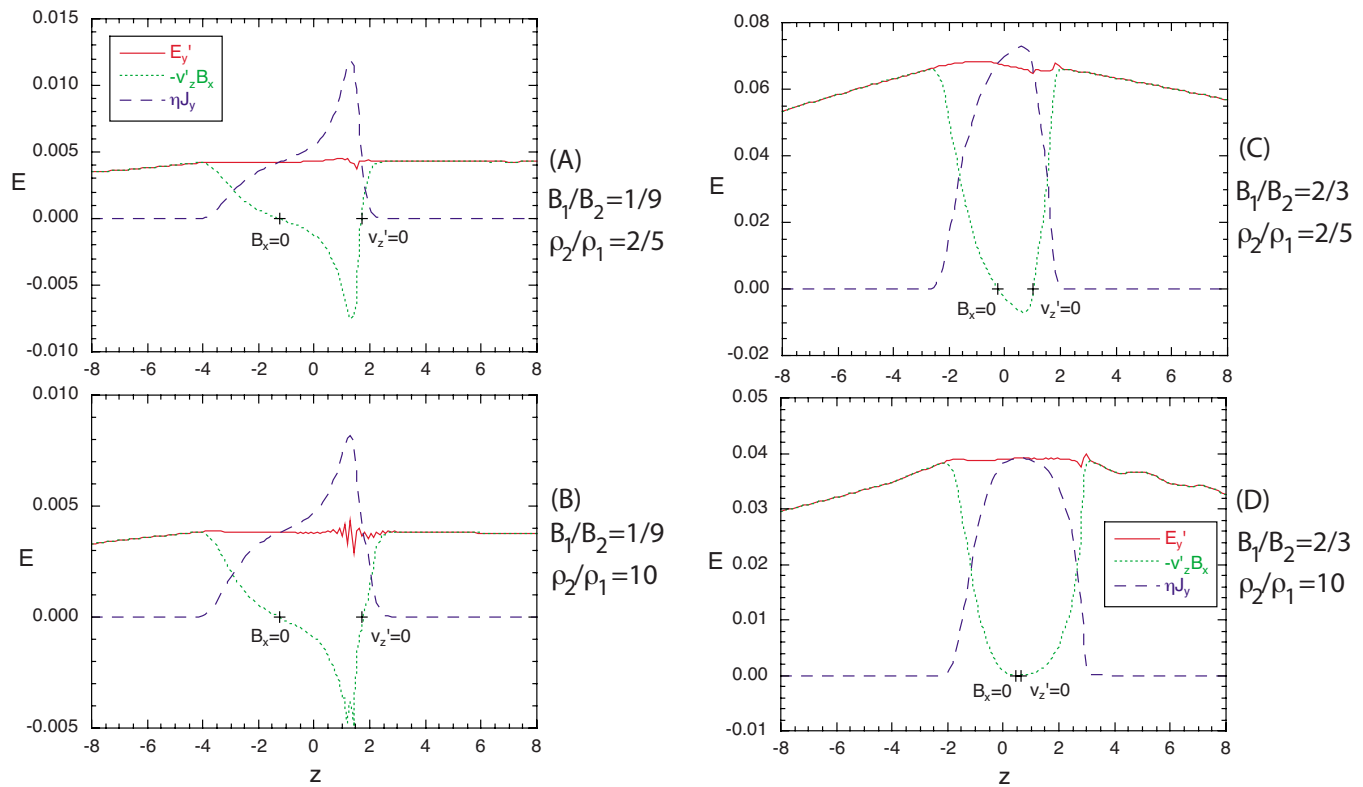


FIG. 8. (Color online) Electric field contributions as functions of z in the vicinity of the reconnection site for nondriven cases A–D, defined in Table I, with $\eta_1=0.5$, evaluated in a frame moving with a speed defined by Eq. (27).

$$v_{0z} = 0.0006, 0.0033, 0.0004, 0.014$$

(for cases A, B, C, and D, respectively), (26)

and (b) by choosing a speed for which the total electric field becomes reasonably flat over the diffusion region,

$$v_{0z} = 0.0022, 0.0025, 0.0004, 0.012$$

(for cases A, B, C, and D, respectively). (27)

The latter case is shown in Fig. 8. Since the instantaneous x-line speed may vary considerably (in case A, for instance, the speed varies between almost zero at the instant considered and an average of about 0.004 over a longer period surrounding this instant), the latter values are more representative of the average x-line speed near the instant considered.

As in Ref. 10, we find that the locations of magnetic neutral line (x-line) and flow stagnation line generally do not coincide, which is related to the fact that the contribution to E_y from $-\mathbf{v} \times \mathbf{B}$ is not only reduced in the diffusion region but even reverses sign. However, we found some disagreement with the prediction by Ref. 10 of the relative locations of x-line and stagnation line. In our simulations the flow stagnation line is in all cases shifted toward the region of higher magnetic field (to the right in Fig. 8), albeit only minimally in case D, both in relation to the x-line and to the center of the diffusion region. The relative locations do not change when the flows are evaluated in the frame of the instantaneous x-line motion, using Eq. (26), rather than the average given by Eq. (27). The separation between the x-line and the flow stagnation line is larger when the ratio between

the magnetic fields of regions 2 and 1 is larger (9:1 for cases A and B). In contrast, Ref. 10 predict the stagnation point is to the left of the x-line in case D and the stagnation point is shifted from the center of the diffusion region toward the side that has lower ρ/B in cases B and D. (Note that, according to the initial values listed in Table I, ρ/B is also slightly lower on side 1, to the left, for case B. However, the actual value just outside the diffusion region is higher, as a result of converging flow.)

We note that, despite the relatively steady appearance of the reconnection rate and the increase in reconnected flux at the times of fastest reconnection (e.g., Fig. 3), true steady states are not attained (see also the discussion in the following section). The electric fields are not fully uniform outside the diffusion region, even in the moving frames.

VII. ENERGY BUDGETS

An important element that is used for the derivation of the scaling of reconnection rates is the energy budget, which may be split up into the following three equations:¹⁵

$$\frac{\partial B^2}{\partial t} = -\nabla \cdot (\mathbf{E} \times \mathbf{B}) - \mathbf{j} \cdot \mathbf{E}, \quad (28)$$

$$\frac{\partial u}{\partial t} = -\nabla \cdot [(u+p)\mathbf{v}] + \mathbf{v} \cdot \nabla p + \eta j^2, \quad (29)$$

TABLE II. Energy flow into and out of the reconnection site for nondriven runs A–D with $\eta_1=0.5$, evaluated at the times of maximum reconnection rate.

		In1	In2	Out	Net
(A)	Poynting flux	0.0041	0.0636	0.0009	−0.0668
	Enthalpy flux	0.7798	0.0162	0.8533	0.0573
	Kinetic energy flux	0.0005	0.0000	0.0450	0.0445
(B)	Poynting flux	0.0039	0.0562	0.0011	−0.0590
	Enthalpy flux	0.8040	0.0142	0.8723	0.0541
	Kinetic energy flux	0.0005	0.0000	0.0163	0.0158
(C)	Poynting flux	0.4349	0.7823	0.1365	−1.0807
	Enthalpy flux	1.1144	0.2152	2.7547	1.4251
	Kinetic energy flux	0.0062	0.0008	0.3806	0.3736
(D)	Poynting flux	0.2395	0.4190	0.0621	−0.5964
	Enthalpy flux	0.6575	0.1080	1.5429	0.7774
	Kinetic energy flux	0.0012	0.0024	0.1541	0.1505

$$\frac{\partial}{\partial t} \frac{\rho}{2} v^2 = -\nabla \cdot \left(\frac{\rho}{2} v^2 \mathbf{v} \right) + \mathbf{v} \cdot (\mathbf{j} \times \mathbf{B} - \nabla p), \quad (30)$$

where $u=p/(\gamma-1)$ is the internal (thermal) energy density, and $\mathbf{E}=-\mathbf{v} \times \mathbf{B} + \eta \mathbf{j}$ in resistive MHD. The terms to the right of the divergence terms of Eqs. (28)–(30) describe the transfer of one form of energy to another; the sum of these vanishes. In a steady state, the terms on the left-hand sides of Eqs. (28)–(30) vanish, such that the sum of the divergence terms must also vanish, describing conservation of the sum of the flux contributions given by

$$\begin{aligned} \mathbf{S} &= \mathbf{E} \times \mathbf{B} \quad (\text{Poynting flux}), \\ \mathbf{H} &= (u + p)\mathbf{v} \quad (\text{enthalpy flux}), \\ \mathbf{K} &= (\rho v^2/2)\mathbf{v} \quad (\text{kinetic energy flux}). \end{aligned} \quad (31)$$

Usually it is assumed that incoming magnetic energy (Poynting flux) is converted mostly or entirely to outgoing kinetic energy.¹⁰ In order to investigate the validity of this assumption we evaluated the energy budget for the four nondriven characteristic cases A–D, defined in Table I. In each case we selected a box $-15 < x < 15$, $-8 < z < 8$ enclosing the reconnection site and calculated the contributions to energy inflow from regions 1 and 2 and the outflow, by integrating the normal fluxes over the inflow and outflow surfaces.

Table II lists these flux contributions, evaluated at the times of fastest reconnection. (Because of the imposed symmetry at $x=0$ only one half of the box, $x>0$, was evaluated.) Since the x-lines are not exactly stationary, we evaluated all fluxes in frames that move with the x-lines, taking the velocities in Eq. (27). The net flow is given by outflow minus inflow. Note that the net fluxes do not add up to zero, due to the time dependence. The fact that all sums are larger than zero is an indication of energy reduction within the chosen box, which was confirmed by investigating the actual changes of the energy content.

As expected from the fact that the magnetic field strength is larger in region 2 and, consequently, the pressure larger in region 1, the inflow from region 1 is dominated by enthalpy flux and the inflow from region 2 by Poynting flux.

Generally we find the expected reduction of Poynting flux and increase of kinetic energy flux, however, these fluxes do not match; the gain in kinetic energy flux is typically less than the loss in Poynting flux. (This effect is even more drastic for the driven cases with the smaller box, not shown here.) Enthalpy fluxes play a significant role in the energy budget. All cases show an increase, comparable to, or even exceeding, the loss in Poynting flux.

The results for the driven cases are generally consistent with the nondriven cases. However, due to the smaller box size and the external driving, there are more oscillations, which makes it more difficult to choose proper box sizes around the reconnection site with a clear distinction of inflow and outflow. In contrast, the results for the nondriven cases shown in Table II do not change significantly if the box size for the evaluation of the fluxes is changed, as long as the major inflows and outflows are included.

We have also evaluated the terms of Eqs. (28)–(30) that describe the transfer from one type of energy to another. In a strict steady state these terms should lead to the same net transfer of energy as listed in Table II. Although our instantaneous states are not strictly time independent, the results from this evaluation, listed in Table III, are qualitatively consistent with the evaluation of the fluxes. In addition, the investigation of the transfer terms reveals that both, Ohmic heating and compressional, adiabatic heating contribute to the transfer from Poynting flux to enthalpy flux. The compressional heating is relatively more important for cases C

TABLE III. Energy transfer terms for nondriven runs A–D with $\eta_1=0.5$, evaluated at the times of maximum reconnection rate; ΔH represents the total transfer to enthalpy flux, column 2 plus column 4, and ΔK the transfer to kinetic energy flux, column 3 minus column 4.

	$\int \mathbf{E} \cdot \mathbf{j} dx dz$	$\int \eta j^2 dx dz$	$\int \mathbf{v} \cdot (\mathbf{j} \times \mathbf{B}) dx dz$	$\int \mathbf{v} \cdot \nabla p dx dz$	ΔH	ΔK
(A)	0.0549	0.0570	−0.0021	−0.0506	0.0064	0.0485
(B)	0.0654	0.0358	0.0296	0.0114	0.0472	0.0181
(C)	1.3920	0.3698	1.0222	0.5697	0.9400	0.0453
(D)	0.7554	0.2332	0.5222	0.3386	0.5718	0.1836

and D; this indicates that cases A and B with the larger ratio between the field strengths on the two sides behave more incompressibly.

VIII. SUMMARY AND CONCLUSIONS

Using resistive magnetohydrodynamic (MHD) simulations, we have investigated asymmetric reconnection in current sheets that separate plasmas with different magnetic field strengths and different densities. We have considered two scenarios, the “Newton challenge” problem,¹³ in which a plane current sheet is deformed by nonuniform external inflow over a limited time, and a nondriven tearing problem, using a much larger simulation box. In both cases we used localized resistivity models, in which the resistivity is confined to the vicinity of the magnetic x-line. By considering asymmetries of both magnetic field strength and resistivity, we extended previous simulation results by Refs. 10 and 11.

Consistent with these previous simulations, we found asymmetric fast outflow primarily aligned with the magnetic field. By considering various inflow parameters, we confirmed that this fast outflow jet goes toward the side with the higher Alfvén speed, rather than higher magnetic field or lower density. The plasma contributing to the fast outflow originates predominantly from the region of higher entropy density or, perhaps, higher pressure.

As in Ref. 10 we found a separation between the x-point and the flow stagnation point; however, in our simulations the latter one was shifted toward the region of higher magnetic field strength rather than towards lower ρ/B as predicted by Ref. 10. While the total electric field is approximately constant over this region, the $\mathbf{v} \times \mathbf{B}$ contribution is not only suppressed in that region but even reverses sign. We note that this effect occurs inside the diffusion region defined by the dominance of ηj . (Reference 10 used uniform resistivity so that the size of this region was determined solely by the scale of j .)

Our results about the relative locations of x-line and flow stagnation line disagree in part with the prediction by Ref. 10. We found that in all cases, relative to the center of the diffusion region (peak of ηj_y), the magnetic x-line was shifted towards the low magnetic field side and the flow stagnation line to the high field side (albeit only minimally for case D with similar magnetic fields but high density ratio between the two inflow regions). The relative location of the x-line and stagnation line was found regardless of whether the flow speed was evaluated in the frame of instantaneous x-line motion or a frame in which the electric field was more nearly uniform, thus being closer to a steady state. (We note that in the latter case the speed of the reference frame was close to that of an average x-line speed over some interval surrounding the instant of consideration.)

This result can be understood from a typical profile of $B_x(z)$, where $B_x=0$ is shifted towards the low field side relative to the maximum gradient, that is, the maximum current density. Since our resistivity is centered around the location of $B_x=0$, this relation is not changed qualitatively when the profile of ηj_y is considered, rather than the current density. (In the case of uniform resistivity they become identical.) In

a steady state, the values of E_y , and thus ηj_y , are the same at the x-line and the flow stagnation line. Hence ηj_y should assume a maximum value in between. This means that the flow stagnation line is shifted toward the high-field side relative to this maximum. We note, however, that this is a plausibility argument only, as the current density profile might deviate from a simple Harris-sheet-type.

For further insight we studied the energy budgets of inflow into, and outflow from, a box surrounding the reconnection site. In addition to the expected reduction in Poynting flux and increase of kinetic energy flux we also found a significant enhancement of enthalpy flux, typically exceeding the increase in kinetic energy flux. This resulted from Ohmic heating as well as adiabatic, i.e., compressional heating. The latter becomes more dominant when the magnetic field strengths on the two sides are closer to each other, i.e., for cases C and D. This predominance of enthalpy flux generation is consistent with earlier simulations of reconnection in the geomagnetic tail.¹⁵

A strong emphasis of this investigation was on the proper scaling of the reconnection rate with the parameters in the two inflow regions. In the collisional MHD regime, this rate also depends on the dissipation, that is, the resistivity. In the high-resistivity regime considered here, however, this dependence weakens and may reach a relatively flat plateau when the Lundquist number, given by Eq. (2), reaches order unity. In that regime the reconnection rates assume magnitudes consistent with Petschek’s model⁴ and with the maximum rates found in collisionless simulations in current sheets of ion inertia scale thicknesses.^{7,13}

To separate this resistivity dependence from the dependence on the external parameters, we considered both of them together with different scalings. Ideally the curves describing the resistivity dependence for various external parameter values should match for the correct scaling. A fairly good agreement was obtained when the approach by Ref. 10 was applied to the regime of fast reconnection by setting $\delta/L=f \approx 0.1$, consistent with Petschek scaling. (Here δ and L are the half-width and the half-length of the dissipation region, respectively.) This is also the approximation used by Ref. 12 in global simulations of magnetopause reconnection, who found good agreement between the estimated and the simulated reconnection rates. In our simulations, a further improvement could be made, when the Alfvén speed for the normalization was based on the actual density ρ_x at the reconnection site, rather than the outflow density estimate derived by Ref. 10. However, even in that case the match was not perfect for the cases considered. There are several reasons for this. (1) Our runs did not assume exact steady states. This was evidenced by spatial variations of the electric field, even in a moving frame taking the x-line motion into account, and by differences between the total energy inflow and outflow, which resulted from a local reduction in energy density. (2) Our investigations revealed a significant role of enthalpy flux generation, typically exceeding the conversion to kinetic energy flux. This conversion was related to the effects of Ohmic heating as well as adiabatic, that is, compressible heating. All of these effects were neglected in the derivation in Ref. 10. The adiabatic heating, associated with

compressibility, becomes more important when the magnetic field strengths in the two inflow regions are comparable in magnitude, regardless of the densities.

ACKNOWLEDGMENTS

This work was performed under the auspices of the U.S. Department of Energy, supported by NASA's Sun Earth Connection Theory and Living With a Star programs, and through a grant from NASA's MMS/SMART program.

¹*Reconnection of Magnetic Fields: MHD and Collisionless Theory and Observations*, edited by J. Birn and E. R. Priest (Cambridge University Press, Cambridge, England, 2007).

²E. N. Parker, *J. Geophys. Res.* **62**, 509, DOI: 10.1029/JZ062i004p00509 (1957).

³P. A. Sweet, *Nuovo Cimento* **8**, 188 (1958).

⁴H. E. Petschek, in *AAS/NASA Symposium on the Physics of Solar Flares*,

edited by W. N. Hess (NASA SP-50, Washington, D.C., 1964), pp. 425–439.

⁵D. Biskamp, *Phys. Fluids* **29**, 1520 (1986).

⁶H. Baty, E. R. Priest, and T. G. Forbes, *Phys. Plasmas* **13**, 022312 (2006).

⁷J. Birn, J. F. Drake, M. A. Shay, B. N. Rogers, R. E. Denton, M. Hesse, M. Kuznetsova, Z. W. Ma, A. Bhattacharjee, A. Otto, and P. L. Pritchett, *J. Geophys. Res.* **106**, 3715, DOI: 10.1029/1999JA900449 (2001).

⁸J. Birn and M. Hesse, *J. Geophys. Res.* **106**, 3737, DOI: 10.1029/1999JA001001 (2001).

⁹A. Otto, *J. Geophys. Res.* **106**, 3751, DOI: 10.1029/1999JA001005 (2001).

¹⁰P. A. Cassak and M. A. Shay, *Phys. Plasmas* **14**, 102114 (2007).

¹¹J. E. Borovsky and M. Hesse, *Phys. Plasmas* **14**, 102309 (2007).

¹²J. E. Borovsky, M. Hesse, and J. Birn, "What determines the reconnection rate at the dayside magnetosphere?" *J. Geophys. Res.* (in press).

¹³J. Birn, K. Galsgaard, M. Hesse, M. Hoshino, J. Huba, G. Lapenta, P. L. Pritchett, K. Schindler, L. Yin, J. Büchner, T. Neukirch, and E. R. Priest, *Geophys. Res. Lett.* **32**, L06105, DOI: 10.1029/2004GL022058 (2005).

¹⁴J. Birn, F. Iino, J. U. Brackbill, and M. Hesse, *Geophys. Res. Lett.* **23**, 323, DOI: 10.1029/95GL03857 (1996).

¹⁵J. Birn and M. Hesse, *Ann. Geophys.* **23**, 3365 (2005).